18th International Conference
ENGINEERING MECHANICS 2012
Svratka, Czech Republic, May 14 – 17, 2012

pp. 1381–1394
Paper #73

ENIGMA OF SUBMERGED FENCE SKIN FRICTION SENSOR

V. Tesař*

Abstract: *The problem with "sublayer fence" skin friction sensor is the disturbance caused by the fence protruding above the surface, however small it is. In an application to the Coanda effect attachment to a curved wall it is known to cause premature transition into turbulence or even flow separation. from the. Author eliminated, already quite a long time ago, these adverse influences in his original version of the sensor with the fence submerged slightly below the surface. Recent detailed investigations revealed the pressure difference output to be dependent on creation of miniature recirculation regions. An attempt to facilitate the recirculation, quite surprisingly, has led to total disappearance of a useful output signal.*

Keywords: ***Skin friction, surface shear stress,***

1. Introduction

Measurement of wall shear stress has been an important – but difficult to perform – part of experimental turbulence research, since the value of this quantity is an indispensable characterisation parameter for description of turbulence. The sudden local increase of the shear stress value taking place in transition from laminar into turbulent character of the flow makes skin friction sensors useful determining the transition position, Tesař (1974). Characteristic feature of contemporary Fluid Mechanics is the progress from mere understanding of fluid flows to controlling them. One of the challenge for the control action is the high turbulent friction. If it were possible to suppress turbulence, efficiency in many fields of activities – from aircraft flight to pipeline transport – would be increased substantially. In principle (although at present neither easy nor economical) it is possible as shown in Ikeda 2007, or Kasagi, Suzuki, and Fukagata 2009 to reduce the friction drag by manipulating the hairpin shaped coherent structures that dominate the near-wall turbulence. The precondition is, of course, detecting the presence of the hairpins. Sensors of local shear stress can perform this task (Grosse and Schröder, 2009). There are two essential requirements the sensor for such application has to meet:

a) its size has to be very small, and

b) must not disturb the flow by its presence.

Other properties, in particular sensitivity, dynamic range of response, and certain robustness are also of importance, but these may be improved upon by development. Most currently used and known methods, however, fail to meet the two basic requirements above, **a** and **b**.

Known methods (their classical but still useful survey is in Rechenberg, 1963) may be sorted into five groups:

1) direct force measurement
2) evaluations from measured velocity profile
3) deformation of inserted second phase (e.g. a liquid on wall in gas flow)
4) piezometric principles generating pressure output signal
5) heat or mass transfer analogy

The ***direct*** method (one of the earliest sources: Dhawan 1953), measuring the extremely small) force acting on a „floating" element of the surface, is generally difficult to use. It is not easy to

* Prof. Ing. Václav Tesař, Institute of Thermomechanics v.v.v.i., Academy of Sciences of the Czech Republic, Dolejškova 5; 182 00, Prague 8; CZ, e-mail: tesar@it.cas.cz

suppress the influence of the pressure forces acting on the element walls in the gaps surrounding the element. It is also extremely difficult to adjust the sensitive alignment of the element surface with the surrounding wall. Solutions of some of these problems is being sought in microfabricated versions, e.g. Shaji, Ng, and Schmidt, 1992).

Measurement of velocity in several points above the surface and use the ***velocity profile*** data is, of course, a typical laboratory technique not suitable for engineering sensors.

Equally limited to the laboratory environment are the methods evaluating the ***deformation*** changes of the geometry of a liquid film applied on the surface exposed to an air flow (Tanner and Blows, 1976, modern version: Desse 2003) - or conversely changes of geometry of a gas bubble in liquid flow.

The ***piezometric*** sensors generate a pressure difference in their output terminals, usually derived from the dynamic pressure on a small body protruding above the surface. These used to be the standard choice for several decades. Typical are Stanton tube (Stanton, Marhall, and Bryant 1920), Preston tube (1053), or sub-layer fence (Konstantinov 1953). The difference is measured by a manometer. Of course, the disturbance to the investigated flow is inevitably significant – especially on a wall of small curvature radius the probe is known to cause premature transition into turbulence or even flow separation.

Considering the disadvantages of the above methods, the interest in a few recent decades has concentrated on the methods based on the analogy between the momentum transfer and the transfer of heat and/or mass. Use of the mass transfer remains somewhat exceptional — the naphtalene sublimation method of Trávníček (Trávníček and Tesař, 2003) can measure the shear stress in principle, but is practically always used to evaluate a different quantity: the total convective transfer rate. This specifically shear stress measurements are now made solely by electrodiffusion method in liquid flows (e.g., Sobolík et al., 1990). In flows of air and other gasses, several practical reasons has led to the current dominance of the ***heat transfer*** principle (Liepman and Skinner G. , 1954, Laghrouche M., et al., 2011). Majority of its users believe the heat transfer method does not disturb the investigated flow. This is a grave mistake: the heating of the wall even by a few degrees can demonstrably influence transition into turbulence and cause flow separation from the wall – as was convincingly manifested by the experiment described by Tesař in 1998.

2. Author's "split-cylinder" sensor

Present author has encountered the problem of the skin friction measurement devices influencing the measured flowfield as long as 40 years ago – Tesař, 1973. The particular flow in question was the Coanda-effect attachment to a strongly curved wall – in the configuration presented in Fig. 1.In this case the influence is particularly strong: even a very small object placed on the surface can change the character of the flowfield completely. The Coanda attachment is also exactly the very case in which the strong sensitivity to even small wall heating was demonstrated by Tesař, 1998. The heating was shown to cause a separation of the attached wall-jet from its attachment wall.

The solution was found in the "split-cylinder" sensor, Tesař 1974 — with no component above the surface (there is no object there - like, e.g., the Stanton tube or the conventional sublayer fence) and no heating. The reason why this approach is now discussed is the fact that it was recently found to be a promising potential component - combined with the high-frequency small-scale fluidic oscillators, described by Tesař, 2012 - of the microfluidic devices that may be used for the suppression of turbulent drag by blowing away from the wall individual hairpin vortices.

The absence of any disturbance in this sensor is possible due to the surprising discovery in 1973 of the fence (like the one at the left-hand side of Fig. 2) generating a useful output pressure signal even if its top edge is submerged to $h < 0$, i.e. under the surrounding surface, as shown at right in Fig. 2.

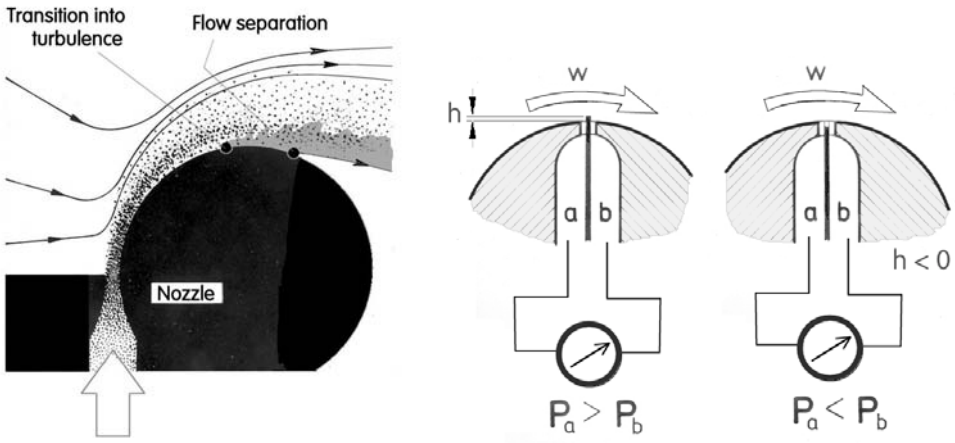

Fig. 1 (Left) The problem that inspired developing the new surface shear stress sensor: Coanda attachment to a curved wall. The sensor is used to detect transition to turbulence and/or separation of the jet from the attachment wall.

Fig. 2 (Right) The disturbance caused by the standard sub-layer fence sensor (at left) can give rise to earlier separation and/or transition. Quite surprisingly (at right), is was found possible to obtain a useful pressure difference signal (of opposite sign) with the fence top submerged below the surrounding surface.

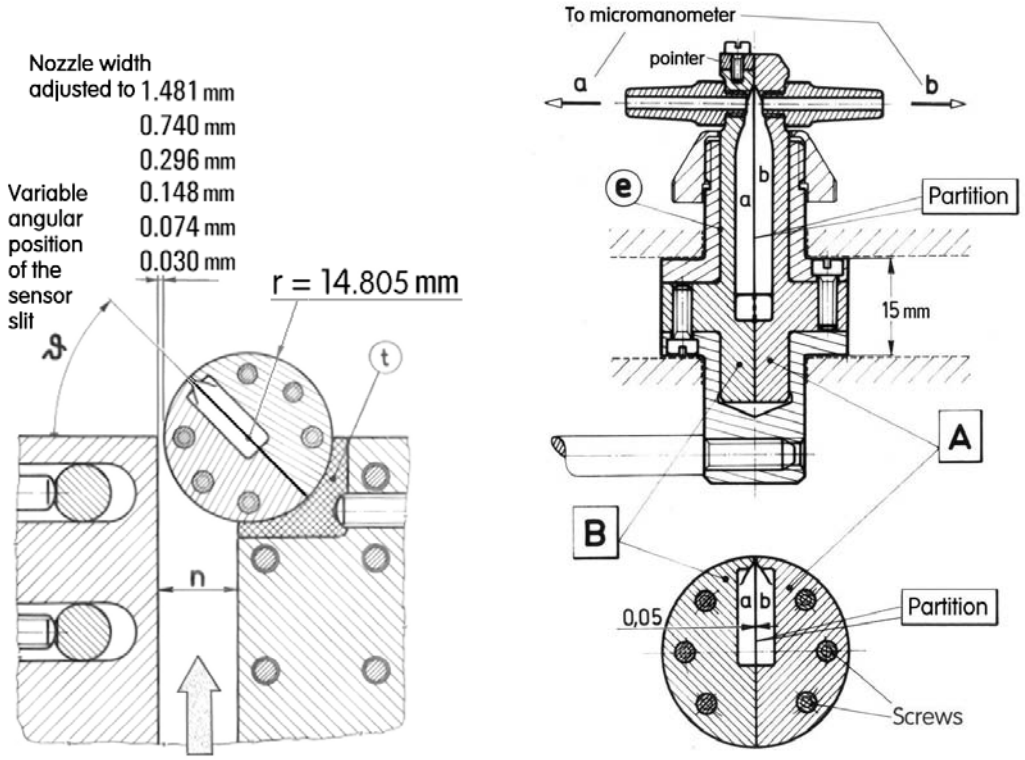

Fig. 3 (Left) Drawing of the central part of the set-up for skin friction measurements under the attached wall-jet. Because of the constant curvature of the attachment wall, the sensor could be positioned to different distances downstream from the nozzle by rotation of the "split cylinder".

Fig. 4 Design of the "split cylinder" component (the attachment wall with the "submerged fence" sensor). The basic part of the cylindrical body consists of two mirror-image parts A and B, separated by 0.05 mm thin metal partition.

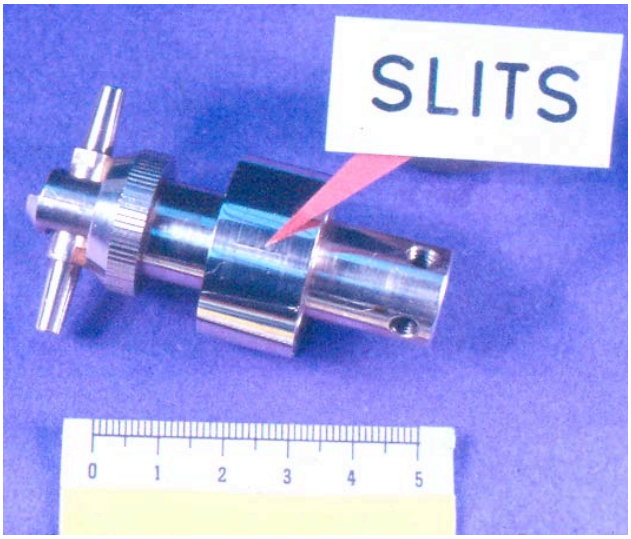

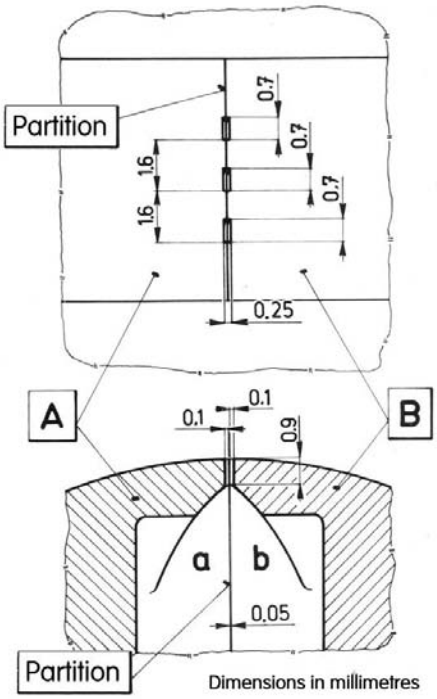

Fig. 5 (Left) Photograph of the "split cylinder" component made according to the drawing in Fig. 4.
Fig. 6 (Right) Detail of the sensing slits geometry.

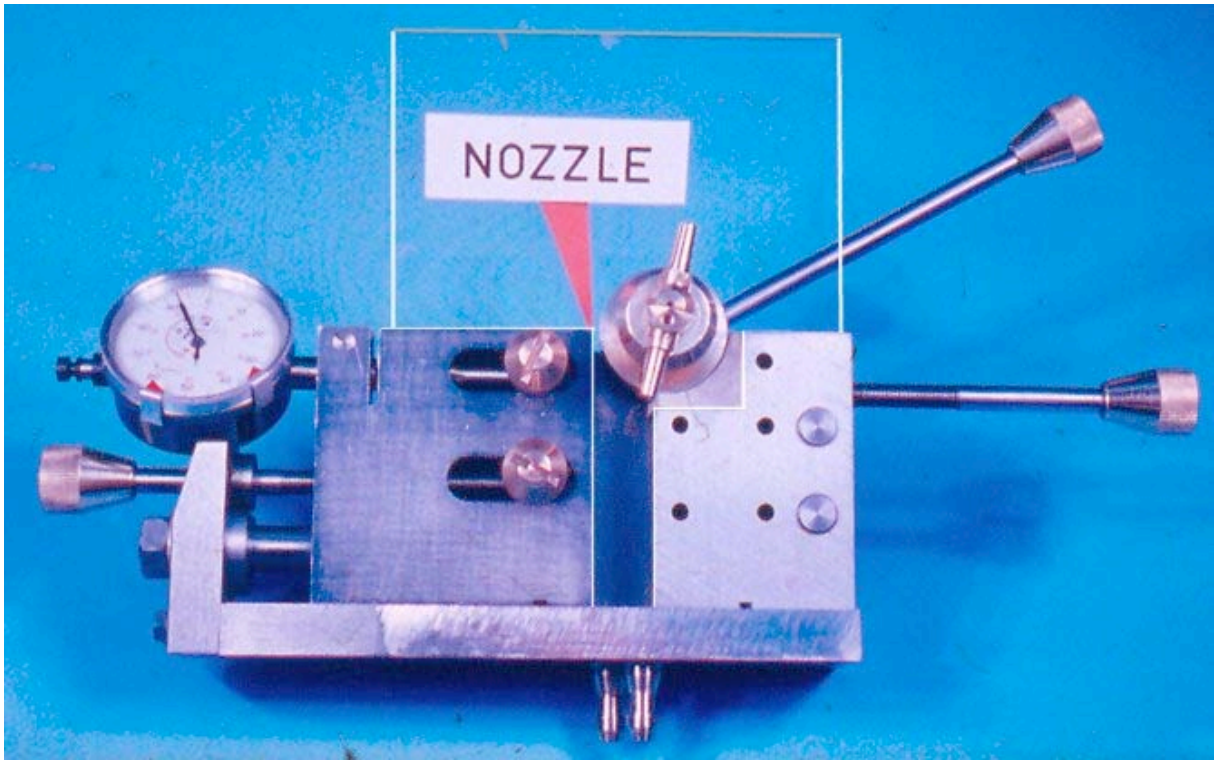

Fig. 7 Photograph of the partly disassembled experimental set-up for investigation of the Coanda-effect attachment. The "split cylinder" component, to which the jet attaches upon leaving the nozzle, is in the centre of the photograph. The curved wall-jet flow takes place between two polymethylemeatcrylate end places, of which only one is in its position here.

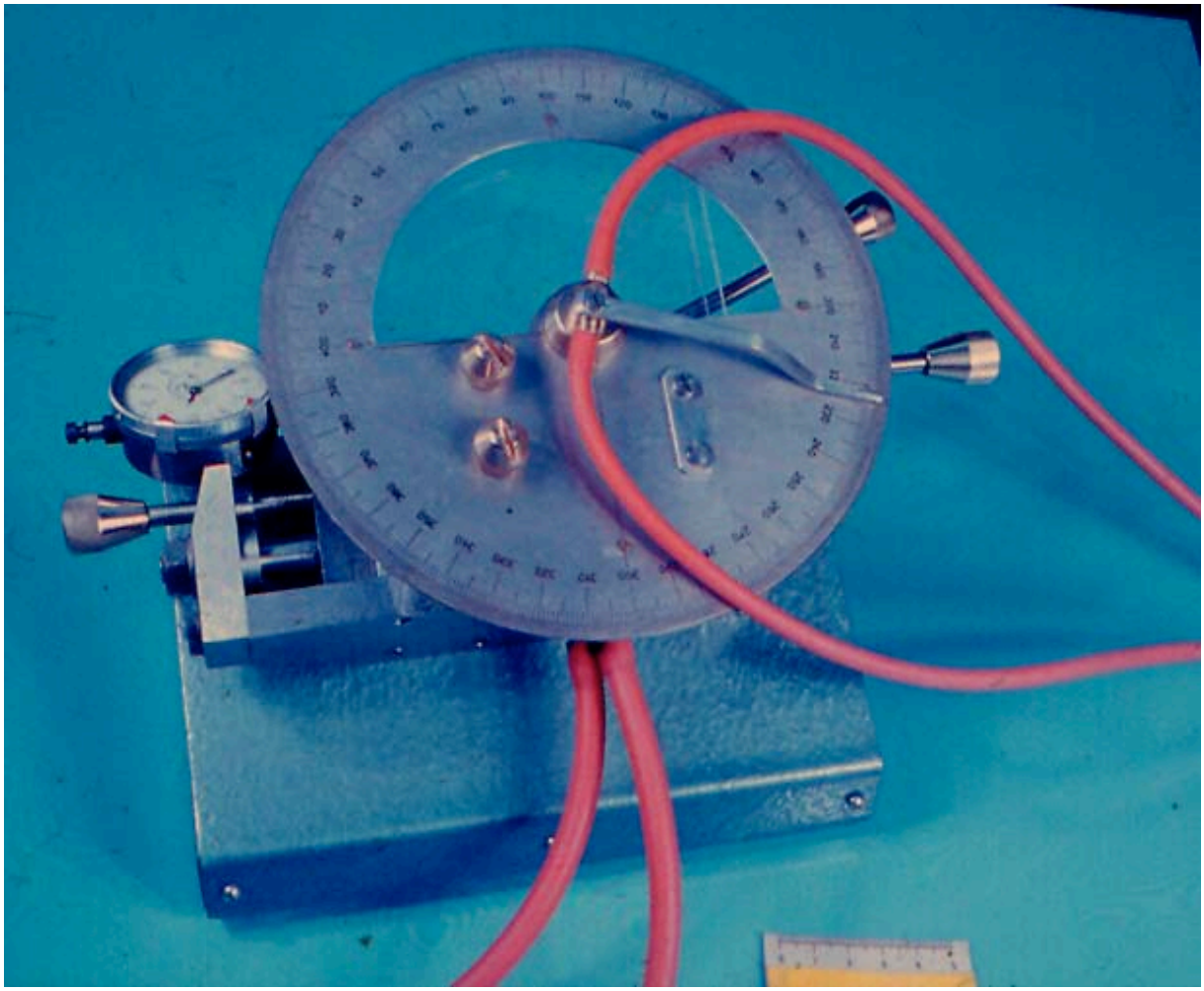

Fig. 8 The experimental set-up assembled. The two bottom rubber tubes supply air into the nozzle, two upper ones carry the pressure-difference signal to the manometer. The angular position of the rotated „split-cylinder" is indicated on the round scale.

The experiment in which this phenomenon was investigated was the Coanda attachment in the set-up shown in Figs. 1, 3, and 7. The flow is a nominally two-dimensional configuration – i.e. with the wall jet bounded on both sides by flat end walls. The important parameter of the attachment, the curvature radius r of the attachment wall, is characterised by its ratio to the nozzle exit width b. As shown in Fig. 3, the radius r in the course of these experiments was 14.805 mm (the decrease from the originally planned 15 mm was due to additional machining of the cylindrical surface necessary to achieve the very high quality) while the width b was adjustable by movement of the left-hand nozzle lip. The values b presented in Fig. 3 indicate that the ratio of the width to the radius r could be set from 0.1 to 0.002. Smaller values mean the nozzle width is so small it is not possible to adjust it with sufficient reproducible precision. On the other hand, larger nozzle width to radius ratios than 0.1 would mean too small nozzle aspect ratio, less than 10, which is not acceptable for the nominal two-dimensionality with the test space bounded by the 15 mm distance between the end walls (Figs. 4, 7).

The fence in the sensor was made from a thin, 0.05 mm foil of phosphor bronze. The foil also served for separation of the cavities through which the pressure difference signals were carried to the manometer. The sensing slits on both sides of the fence - upstream and downstream – were very narrow, of 0.1 mm width (Fig. 6). This small size made possible high spatial resolution of the investigated transition positions. The sensor did not span the full 15 mm height of the cylindrical attachment wall between the plexiglass end plates; its length perpendicular to the flow direction was only 0.7 mm (Fig. 6) to avoid possible bending of the very thin fence by the acting pressure difference in some extreme regimes. To increase sensitivity, there were actually three sensors side by side, operating in parallel: apart from the central one in the middle of the cylindrical attachment wall height there was another sensor on its both sides, separated by the 0.9 mm wide flat surfaces, well

seen in Fig. 10. In the initial verification tests, it was quite surprisingly possible to receive a useful output pressure difference signal from the sensor with the fence machined flush with the surrounding cylindrical surface. However, the measured pressure difference ΔP in these tests with the nominally zero fence height h was of the opposite sign to the standard output signal of the sublayer fence method. Visual inspection at a very large magnification made this sign reversal comprehensible: the machining on a lathe caused the top of the fence – exposed in the 0.7 mm wide sensing slits unsupported to the machining tool - to be cut away more than the surrounding surface. Obviously, the machining made unintentionally the configuration to become actually the one with the " submerged", negative height h fence (right-hand part of Fig. 2).

The accompanying drawings (Figs. 3, 4, and 6) and the photographs (Figs. 6, 7, 8, 9, 10, and 11) provide all the information about the design of the shear stress sensor, used for measurement of the skin friction on the surface of the "split cylinder" . The cylinder actually consisted of two separately made symmetric halves, A and B, with the thin 0.05 mm phosphor bronze partition between them. The three sensors arranged in parallel (Fig. 6, 10, 11) were on both sides connected to the common outlet channels (a and b) indicated in the drawing Fig. 4 and well visible in the photograph Fig. 9.

The cylindrical core body with the three sensors was used in the experimental set-up the design of which is apparent from Figs. 3, 7, and 8. The cylinder was adjusted to different angular positions, read on the large circular scale in Fig. 8.

The " split-cylinder" sensing method, being indirect, necessitated performing a calibration prior to the actual measurements. Because of the cylindrical geometry, the calibration could use the Blasius solution of laminar boundary layer on a cylindrical surface. Again, the output pressure difference measurements were made at various angular positions relative to the parallel flow in a wind tunnel. To get nearer to the assumed infinite length of the cylinder, the sensor part was provided with extensions (Figs. 12, 13, and 14). The assembly is seen tin the test section of the wind tunnel in Fig. 15.

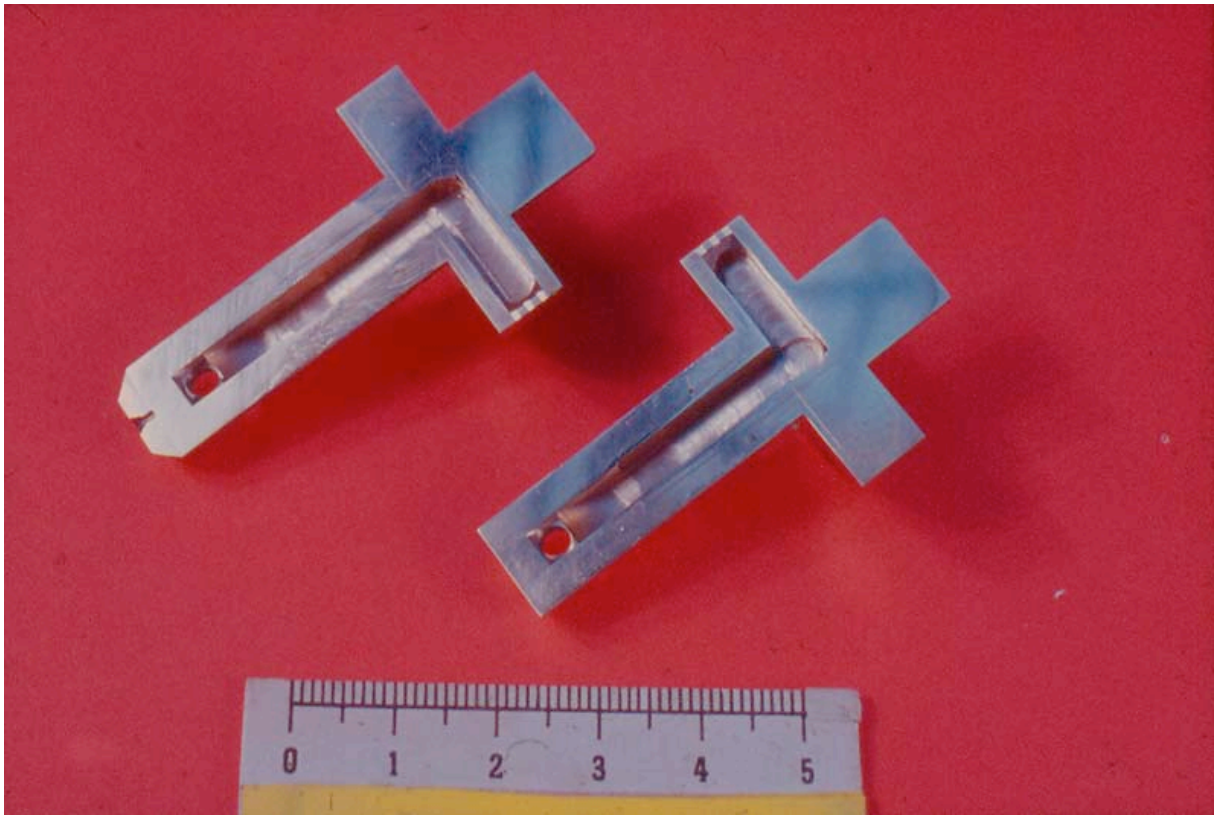

Fig. 9 The key parts A and B (cf. Fig. 4, 6) of the "split cylinder". The two components are mutual mirror images; the milled cavities for transfer of the pressure difference signal to micro-manometer are in the assembled state separated by the phosphor-bronze partition (not shown here).

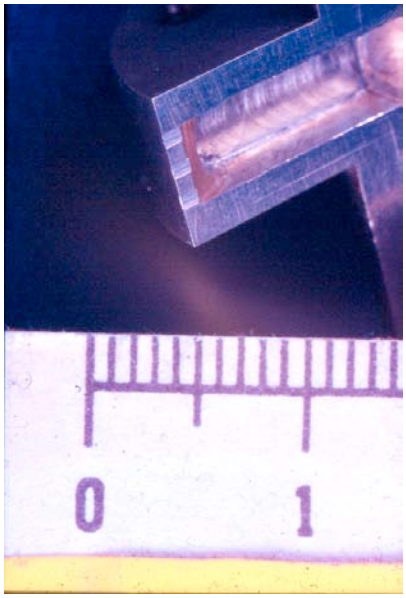

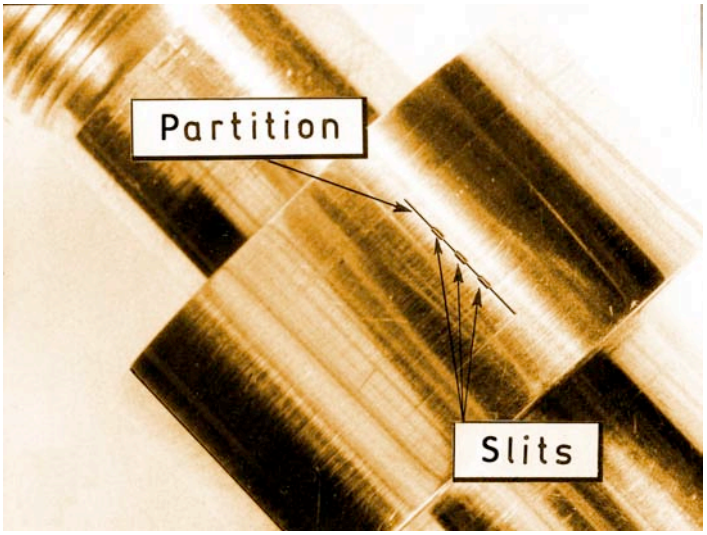

Fig. 10 (Left) Detail photograph of the grooves that form sensing slits.

Fig. 11 (Right) The sensing slits as they were actually used in subsequent measurement: the external edge of the partition was machined to be nominally flush with the surface of the surrounding parts A and B, but lack of support during the machining operation resulted in this edge being slightly lower inside the slits.

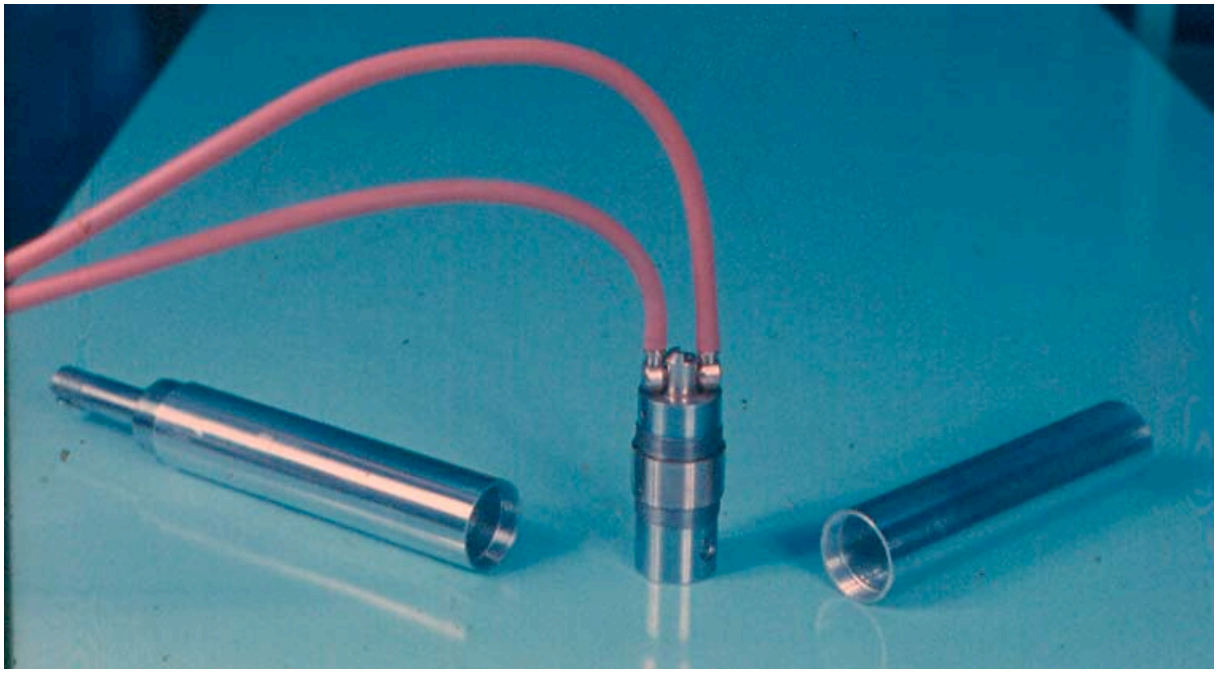

Fig. 12 For calibration in the wind tunnel, the „split cylinder“ component was provided with extensions that converted the assembly into a constant-diameter cylinder body spanning the tunnel test section.

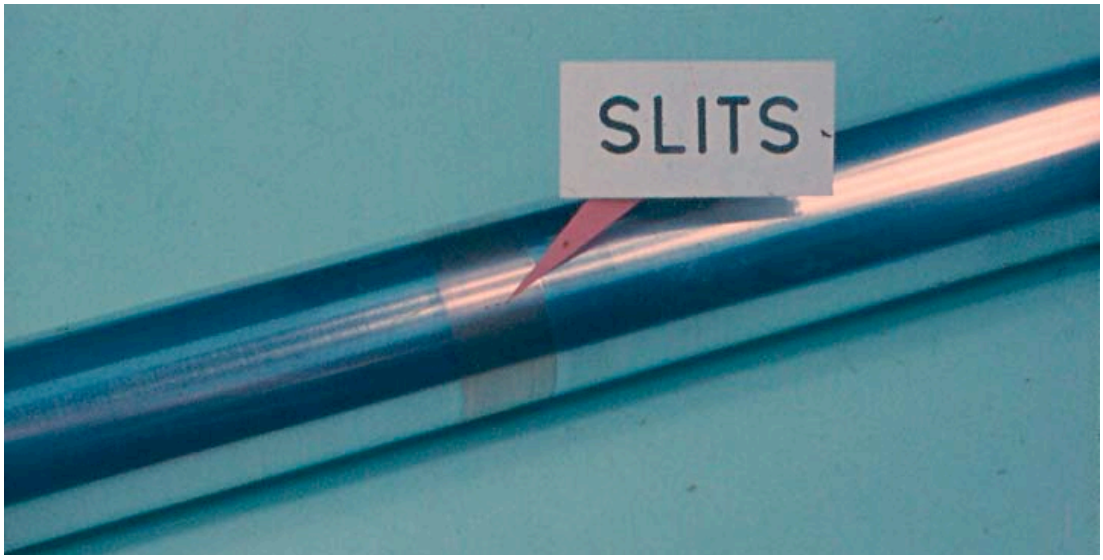

Fig. 13 (Right) Detailed photograph of the surface of the component M (see the next Fig. 14) and the flush fitting extensions. The diameter to length ratio of the complete assembly was satisfactory d / l = 0.1057 so that the local surface shear stress may be calculated from the known Blasius boundary layer solution for infinitely long round cylinder.

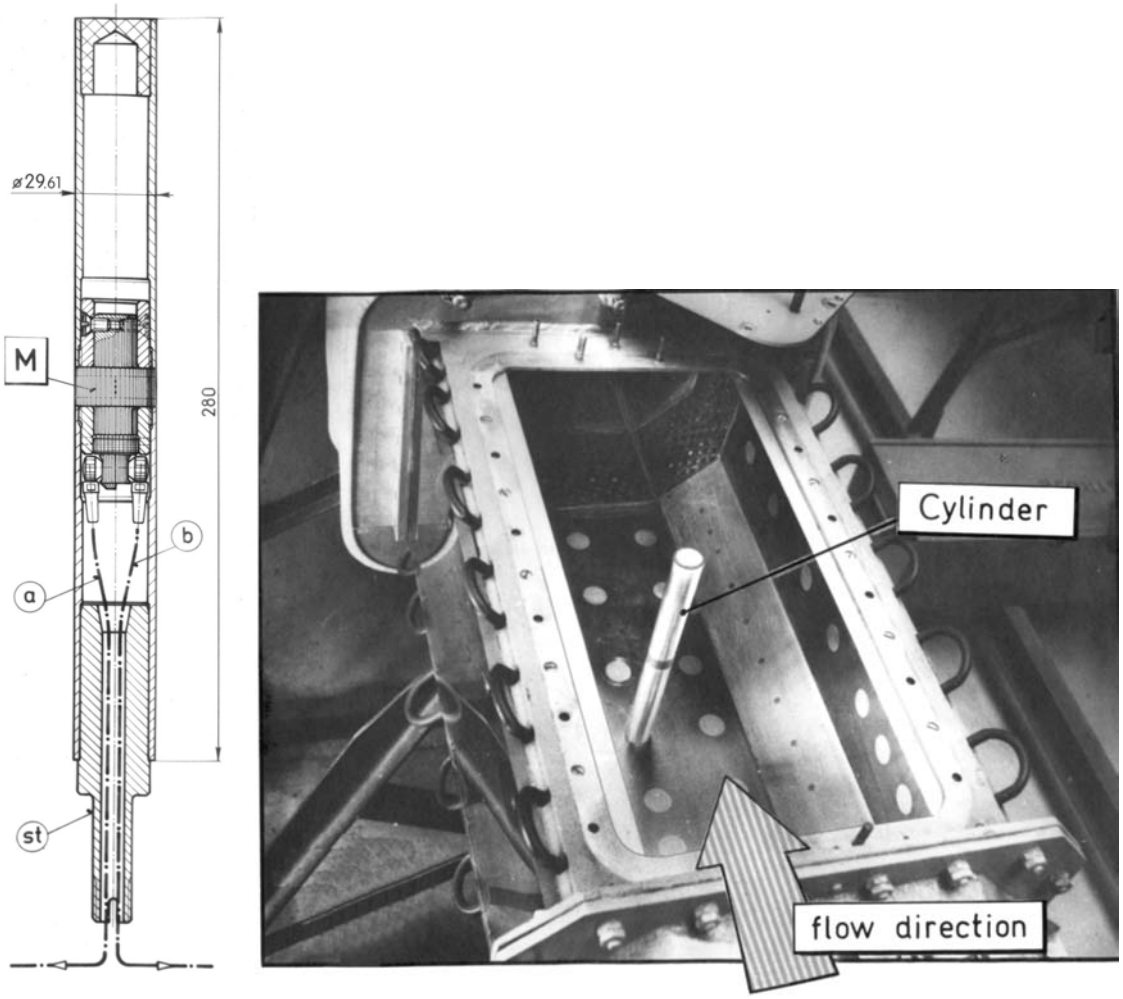

Fig. 14 (Left) Drawing presenting the internal layout of the cylinder with the central component M and the fitting extensions.

Fig. 15 (Right) Photograph of the cylinder body as shown in Fig. 14 positioned in the wind tunnel test section. The blockage ratio of the cylinder diameter to the test section width was 0.075, small enough for neglecting any blockage corrections.

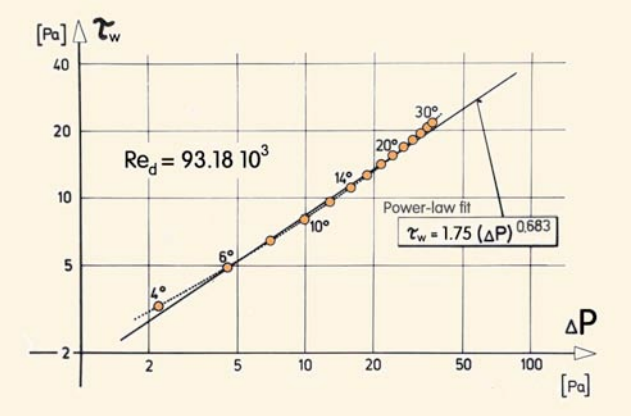

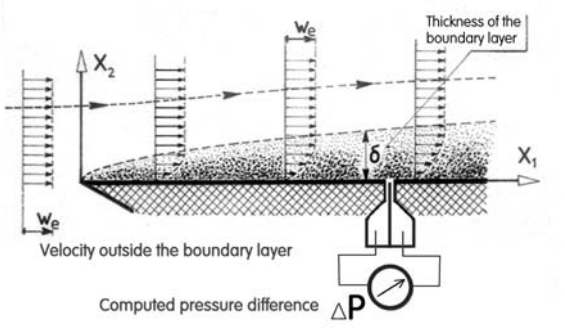

Fig. 16 (Left) An example of the dependence obtained in one of the calibration runs. The wall shear stress τ_w is calculated from the Blasius solution, the pressure difference ΔP in the sensor output was measured by a 1:50 inclined tube Rosenmüller alcohol micromanometer.

Fig. 17 (Right) Configuration of the numerical flowfield solutions: the sensor is positioned at several downstream locations X_1 from the leading edge of a flat plate laminar boundary layer.

Calibration runs in the wind tunnel were made at six different Reynolds numbers (i. e. six wind tunnel flow velocities). An example of the typical measurement run (with a polynomial fit) is presented in Fig. 16. The computed wall shear stress τ_w was in the range from 1 Pa to 50 Pa, the corresponding measured output pressure differences ΔP were within the range from 0.5 Pa to 100 Pa. The results of all six calibration measurement runs could be fitted reasonably by a single calibration dependence.

It seemed obvious that the mechanism of the sensing is associated with the standing vortical structures one can imagine to form in the entrances of the sensing slits. The details of the mechanism, however, remained unexplained. This was a grave hindrance in a way towards obtaining desirable higher sensitivity.

What seemed to be a plausible proposition was that an improvement in the output signal levels should be possible by providing more space for the standing vortical structures so that the air there could recirculate more freely. The simplest way how to provide this space was retracting the fence somewhat more (i.e. to get a higher absolute value of the negative height h, Fig. 2). Unfortunately, contrary to the expectation, instead of an improvement the measured pressure difference after such adaptation was found practically independent of the acting skin friction, making the sensor useless. This fact has shown that the basic concept of the sensor followed so far was obviously incorrect.

3. Numerical flowfield computations as a way towards understanding the flow

Obtaining more insight into the sensor working mechanism experimentally, by observations and direct tests, was not possible because of the sensor inaccessibility during operation and its extremely small size. It was therefore decided to get more information by performing numerical computations of the flowfield inside the sensor inlet space. It should be emphasised that there was no intention to perform the computations in a way simulating the conditions in the "split-cylinder" sensor — even though the size of the sensor duplicated the b = 0.25 mm dimension with the 0.05 mm thick fence. The aim was to demonstrate the reality of generating of the output pressure difference with the submerged fence h < 0 and possibly to find the ways towards a performance improvement, using as the guide the computed internal conditions in the sensor entrance and its vicinity. For this purpose, it was considered preferable leave aside the somewhat special case of the Coanda attachment as well as the effects of wall curvature and to perform the computations in the flat-plate boundary layer flow, as shown in Fig. 17. This, of course, was likely to provide more general conclusions.

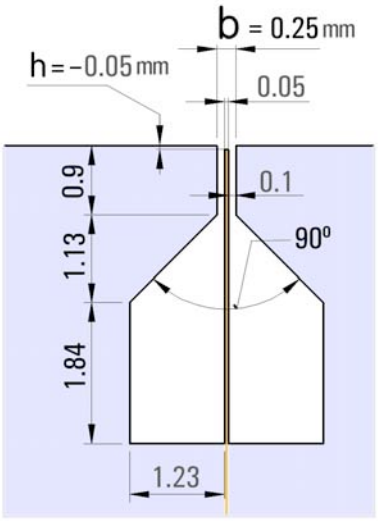

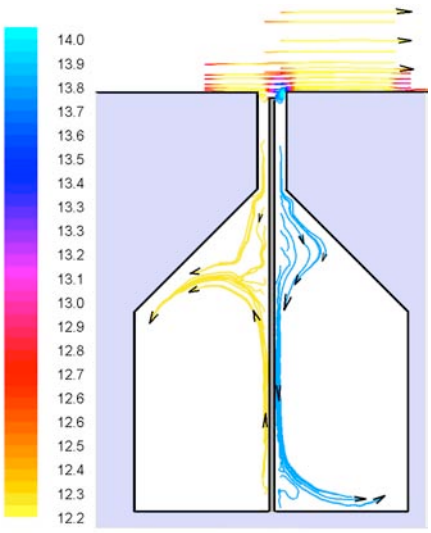

Fig. 18 (Left) Geometry of the sensor used in the computations. The negative height h *of the top of the fence was varied; the results presented here were obtained with* $h = -0.2\ b$ *(shown in this illustration) and* $-0.4\ b$*. The output pressure values were read at the bottom of the two cavities.*

Fig. 19 (Right) Computed pathlines inside the sensor cavities show the induced vortical motions with opposed directions at the partition surface. The velocities of these motions, however, are too slow for this phenomenon having any practical significance.

The computation domain was two-dimensional, with flow in rectangular space 580 mm long and 80 mm high, the boundary layer formed on the domain bottom. The geometry of the sensor as used in the first computation series (later series were made with slightly varied geometry) is presented in detail in Fig. 18: the top of the fence was chosen to be 0.05 mm below the top of the wall – the wall at which was generated the laminar boundary layer. The used solver operated with pressure-based implicit formulation, and assumed laminar flow (because even if used in turbulent flows, the sensor works in the viscous "laminar" sublayer). Initially, the sensor was placed at the streamwise distance $X_1 = 500$ mm from the leading edge. — i.e. sufficiently far on all sides from the boundaries of the computation domain. In some later computations, the sensor entrance was also positioned at streamwise distances 400, 300 and 200 mm. The working fluid was air with specific volume $v = 0.8163\ m^3/kg$ and kinematic viscosity $\nu = 14.6073\ 10^{-6}\ m^2/s$. The boundary conditions were the constant velocity w_e everywhere along the entrance at left, which was 80 mm high. The same also constant velocity w_e was demanded to prevail over the whole top of the domain (80 mm above the bottom solid wall). These velocities were varied to be different in different computation runs, in the range from 3 m/s to 15 m/s (rather small values in agreement with the assumed laminar flow character). In the exit from the domain, at 580 mm horizontal distance from the leading edge, the condition was an everywhere constant, atmospheric pressure.

The domain discretisation was by unstructured triangular elements, the number of which was gradually increased in the course of the computation by refinement in the regions with static pressure gradient above a gradually decreased limit value. Typical final number of the discretisation cells in the final, converged state of the solution was ~ 200 000 cells and ~ 300 000 triangle sides, the typical limiting (highest) value of the gradient was 0.0028 Pa/mm. The computation was considered converged if the solved relative residua of all equations were below 10^{-6}. The 80 mm height of the domain was more than sufficient to accommodate the test shear flows, since typical boundary layer thickness above the sensor was $\delta = 13.6$ mm (the highest value encountered in the course of the whole computation series was $\delta = 19.95$ mm).

The geometry of the sensor cavities, simulating the chambers of the pressure transducer, did not have practically any influence on the computed output pressure difference $\triangle P$ (with the higher pressure in the downstream cavity). The computations actually revealed, as shown in Fig. 19, that there was an upwards flow past the downstream face of the partition and an opposite downwards flow

past the upstream face of the fence. These directions correspond to the character of the generated pressure difference $\triangle P$ in the output terminals - nevertheless the velocities involved were extremely slow and unlikely to result in a practically significant pressure effect. Of more importance are the pressure minimum an maximum that were found in the performed computations — Fig. 20 — at the entrance and exit corners, respectively, of the sensor entry . The pressure values correspond to the colourbar at left in Fig. 20.

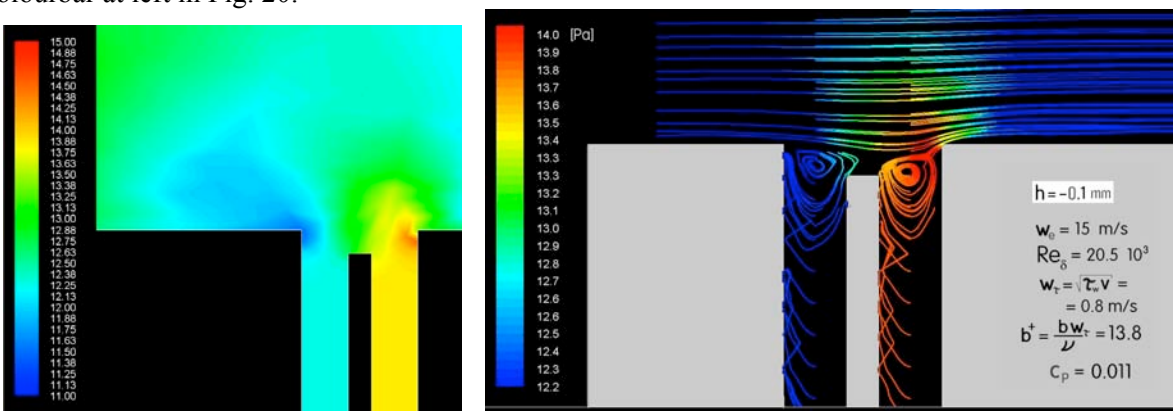

Fig. 20 (Left) An example of computed pressure field near the sensor entrance. The computations suggest the pressure differences measured by the sensor are generated in the flows past the entrance corner at left and the exit corner at right, respectively. The colourbar shows values of pressure relative to the domain exit.

Fig. 21 (Right) Typically for the configurations generating the reasonable pressure signal, also in the $h = -0.2\ b$ *case presented here, the computed pathlines show existence of two separate vortices in the two sensor entrances.*

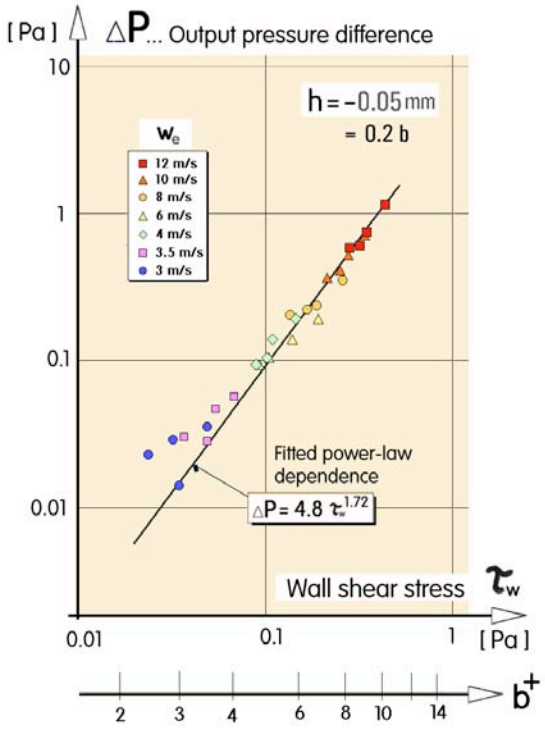

Fig. 22 Results of the large number of performed computations: dependence of the sensor output pressure difference $\triangle P$ *on the shear stress* τ_w *, the latter evaluated from the slope of the velocity profile at the wall. The auxiliary scale below indicates very small magnitude of the sensor entrance width* b *when evaluated in the friction co-ordinates.*

What was the most important phenomenon shown by these computations is the character of fluid motion inside the entrance, as shown in Fig. 21. As expected, it is a motion of vortical character. What was perhaps not expected is there are two, co-rotating mutually non-communicating standing vortices.

As the numerical results of performed computations is presented in Fig. 22 the dependence between the generated output pressure difference $\triangle P$ and the wall shear stress τ_w. The latter was evaluated from the slope of the computed velocity profile one wall in the vicinity of the sensor entrances. Perhaps more important than the evaluated overall dependence (power-law expression fitted to the data — which is valid for the simplified case chosen for obtaining the insight into the mechanism rather than to model any particular real sensor) are the values of the corresponding sensor entrance width b converted into the friction co-ordinates:

$$b^+ = \frac{b w_\tau}{\nu} = \frac{b}{l_\tau} \qquad ...(1)$$

These values may be read on the auxiliary scale at the bottom of Fig. 22.

Conditions on a solid surface influenced by prevailing shear stress τ_w [N/m^2 = Pa] are characterised by *friction velocity* w_τ [m/s] — a quantity evaluated as

$$w_\tau = \sqrt{\tau_w v} \qquad ...(2)$$

where v [m3/kg] is the specific volume of the fluid. The scales of the coherent structures in turbulence - and consequently also the devices used for their detection - are characterised by the friction length, evaluated as

$$l_\tau = \nu / w_\tau \qquad ...(3)$$

where ν [m^2/s] is the fluid kinematic viscosity.

A typical hairpin vortex has its two arms of diameter $30\text{-}40\ l_\tau$ and length $\sim 10^3\ l_\tau$. It is commonly estimated that the sensor capable to detect these vortices should be smaller than about $30\ l_\tau$. The auxiliary scale at the bottom of Fig. 22 shows that in spite of the size of the investigated sensor example chosen as being manufacturable by standard large-scale machine tools, this condition of the sensor smaller than $30\ l_\tau$ is more than sufficiently fulfilled (in fact leaving actually ample reserve for further miniaturisation).

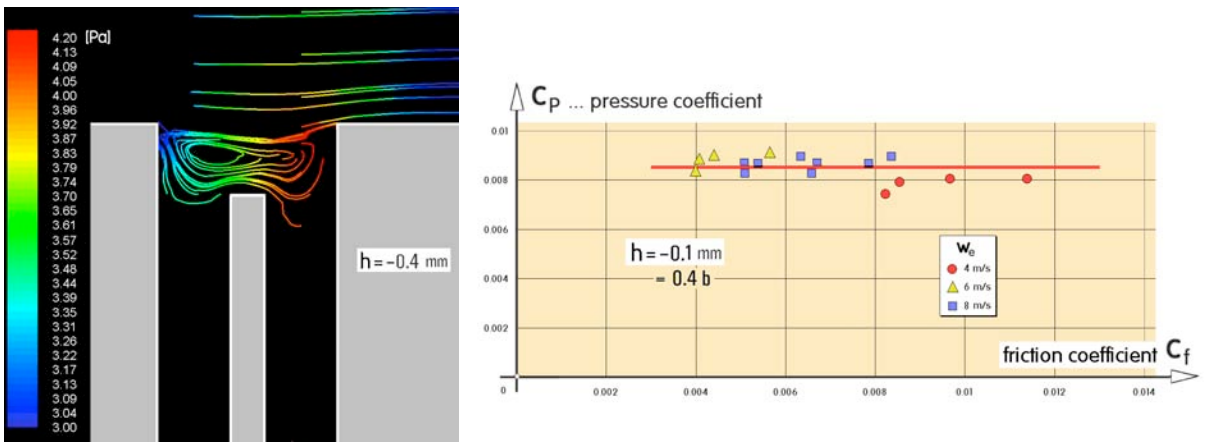

Fig. 23 (Left) Typical computed pathlines for the larger cavity - increased over the previous geometry from Figs. 18 and 21 by moving the fence downwards to $h = -0.4\ b$. This makes easier the vortical motions in the sensor entrance – but makes it possible for the two vortical motions (Fig. 21) to unite and form just a single larger vortex.

Fig. 24 (Right) Contrary to the expectations, the results show practically constant output pressure (here presented in terms of pressure coefficient c_P) irrespective of the variations of the wall shear stress (characterised by the friction coefficient)..

4. The enigma of single vortex

Early thoughts about the operation mechanism of the submerged fence sensor led to the conviction that the fluidic output signal could be increased by giving more free unconstrained space to the generation of the standing vortices in the sensor entrance. The simplest way how to do it is obviously further retraction of the fence, making larger the unobstructed space above the fence top. However, as mentioned already above, the simple tests made with the sensor model failed to bring the expected improvement: on the contrary, the measured pressure difference after moving the fence slightly down have shown the output pressure difference $\triangle P$ independent of the acting shear stress τ_w.

In an attempt at getting an insight into the reason fro this surprising behaviour, the computations were extended to the configuration differing only in the height h in Fig. 18 changed to $h = -0.4$ mm. The resultant dependence of the generated output pressure difference $\triangle P$ on the wall shear stress τ_w is presented in Fig. 24 – in terms of the corresponding pressure coefficient

$$c_p = \frac{2\,v\,\triangle P}{w_e^2} \qquad ...(4)$$

and friction coefficient

$$c_f = \frac{2\,v\,\tau_w}{w_e^2} \qquad ...(5).$$

It is obvious that, as in the laboratory tests with the sensor, this adaptation of the fence height resulted in loss of the capability to measure the shear stress τ_w.

Because the computations were made by the same procedures with the identical boundary conditions and other parameter values as those described in the previous section it is quite probable that this surprising result is not due to some mistake made in the numerical solutions and reflects some real change in the character of the flowfield past the sensor entrance.

A detail of the computed flowfield displayed again by means of the calculated pathlines presented in Fig. 23 shows that the only – but substantial - change when compared with the previous results is the two vortices from the analogous Fig. 21 have here coalesced into a single flat vortex. This, however, does not seem to be a reason for the apparent equalisation of the pressure values in the two pressure-reading cavities.

5. Conclusions

Experiments as well as performed numerical flowfield computations have demonstrated that the submerged fence skin friction sensor, having the exceptional property of causing a minimal disturbance to the investigated flow, can operate and generate a useful measurable output fluidic signal at extremely small dimensions – less than those discussed in literature as being capable of discriminating the dissipative vortical structures in turbulent boundary layers. The computations made with the intention to understand the mechanism of generating the output pressure difference by the vortical motion in the sensor entrance did provide some answers, but failed to explain the enigma of the pressure difference loss with the more submerged fence.

Acknowledgement

Author expresses his gratitude for the support by the grant 101/11/J019 donated by GAČR, and by grant TA02020795 received from the Technological Agency of the Czech Republic, programme ALPHA.

References

Desse J. M. (2003) Oil-Film Interferometry Skin-Friction Measurements under White Light, *AIAA Journal*, Vol. 41, p. 2468

Dhawan S. (1953) *Direct Measurements of Skin Friction*, NACA Report 1121, p. 281

Grosse S., Schröder W. (2009) Wall-Shear Stress Patterns of Coherent Structures in Turbulent Duct Flow, Journal of Fluid Mechanics, Vol. 633, p. 147, 2009

Ikeda K. (2007) Trends in Research on Turbulence Control Aiming at Reducing Friction Drag, *Science and Technology Trends Quarterly Review*, No. 22, p. 98

Kasagi N., Suzuki Y., Fukagata K.. (2009) Microelectromachnical Systems-Based Control of Turbulence for Skin Friction Reduction, *Annual Review of Fluid Mechanics*, Vol. 41, p. 231

Konstantinov N. I (1953) Comparative Investigation of the Friction Stress on the Surface of a Body (original in Russian, Translated 1960 DSIR RTS 1499), *Energomashinostroenie*, Vol. 176, p. 201

Laghrouche M., et al. (2011) In Situ Calibration of Wall Shear Stress Sensor for Micro Fluidic Application, *Proc. of Conf. „Eurosensors XXV"*, Athens, Greece, 2011

Liepman H., Skinner G. (1954) Shearing Stress Measurement by Use of a Heated Element, *NACA TM 3268,* 1954

Preston J. H. (1953) The Determination of a Turbulent Skin Friction by means of Pitot Tubes, *Journal of the Royal Aeronautical Society*, Vol. 58, p. 109

Rechenberg I. (1963) Messung der turbulenten Wandschubspannung (Measurement of wall shear stress — in German), *Zeitschrift für Flugwissenschaften*, Vol. 11, p. 429

Shaji J., Ng K.-Y., Schmidt M. A. (1992) A Microfabricated Floating-Element Shear-Styress Semsor Using Wafer-Bondong Technology, *Journ. of Microelectromechanical Systems*, Vol. 1, p. 89

Sobolík V., Wein O., Gil O., Tribollet B. (1990) Three-Segment Electrodiffusion Probes for Measuring Velocity Fields Close to a Wall, *Experiments in Fluids*, Vol. 9, p. 43

Stanton T. E., Marshall D., Bryant C. N. (1920) On the Conditions at the Boundary of a Fluid in Turbulent Motion, *Proc. of the Royal Soc. (A)*, Vol. 97, p. 413

Tanner L. H., Blows L. G. (1976) A Study of the Motion of Oil Films on the Surfaces in Air Flow, with Application to the Measurement of Skin Friction", *Journal of Physics E: Scientific Instruments*, Vol. 9, p. 194

Tesař V. (1973) Experimentální vyšetřování přilnutí proudu tekutiny k zakřivenému povrchu (Experimental Investigations of fluid jet attachment to a curved surface – in Czech), *ACTA POLYTECHNICA - Práce ČVUT v Praze* II, 5

Tesař V. (1974) The 'Split-Cylinder' Sensor for Skin Friction Measurement in Curved Wall-Jet Flows, *Proc. of the Vth 'Jablonna' Fluidics Conference*, p. 17, Budapest, Hungary

Tesař V. (1998) Control of Flow Separation by Temperature Gradient, *Proc. of Euromech Colloquium 377 "Stability and Control of Shear Flows with Strong Temperature or Density Gradients"*, p. 54 , ISBN 80-85918-43-9, Prague

Tesař V. (2012) High-Frequency, Small-Scale Fluidic Oscillators for Boundary Layer Control, *Proc. of Conf. 'Topical problem of Fluid Mechanics 2012*', Inst. of Thermomechanicvs AS CR, Prague

Trávníček Z., Tesař V. (2003) Annular synthetic jet used for impinging flow mass transfer, *International Journal of Heat and Mass Transfer*, Vol. 46, p. 3291